Supplementary Information (SI) for Energy & Environmental Science.

Supporting Information

Enhanced electrical performance of perovskite solar cells via strain engineering

Siyang Cheng[1,2,5], Yuanhang Yang[1,2,5], Xueliang Zhu[1,2,4,5], Yahui Li[3], Hao Li[1,2], Wenqi Xiong[1], Zhuo Zheng[1,2], Sheng Li[1,2], Yong Liu[1], Xiaoze Liu[1], Qianqian Lin[1], Shengjun Yuan[1,2], Enzheng Shi[3], Zhiping Wang[1,2*]

[1]School of Physics and Technology, Key Lab of Artificial Micro- and Nano-Structures of Ministry of Education, School of Microelectronics, Wuhan University, Wuhan, China

[2]Wuhan Institute of Quantum Technology, Wuhan, China

[3]Research Center for Industries of the Future and School of Engineering, Westlake University, Hangzhou, China

[4]College of Science, China Jiliang University, Hangzhou, 310018, China

[5]These authors contribute equally to this work

[*]E-mail: zp.wang@whu.edu.cn

Methods

Materials

All the materials were used as received without purification. *N*, *N*-dimethylformamide (DMF, 99.8 %), dimethyl sulfoxide (DMSO, 99.7 %) and Nickel (II) acetylacetonate [Ni(acac)$_2$, 95 %] was purchased from Sigma Aldrich. Formamidinium iodide (FAI, 99.99 %) and methylammonium iodide (MAI, 99.99 %) were purchased from Great Cell Solar. Caesium iodide (CsI, 99.9 %) was purchased from Alfa-Aesar. Lead iodide (PbI$_2$, 98 %) and [4-(3,6-Dimethyl-9H-carbazol-9-yl) butyl] phosphonic acid (Me-4PACz, 99%) were purchased from TCI. 3-fluoro-phenethylammonium iodide (3F-PEAI, ≥99.5%) and methylammonium chloride (MACl, ≥99.5%) was purchased from Xi'an Polymer. Buckminsterfullerene (C60, 99.5 %) was purchased from Nano-C. Hydrochloric acid (HCl) was purchased from Sinopharm. All other solvents were anhydrous and purchased from Across Organic. The FTO coated glass was purchased from Suzhou Shang Yang Solar Technology Co., Ltd. The synthesis of 2TI is detailed in earlier reports[1,2].

Device fabrication

The FTO substrates (2.5 × 2.5 cm, 7 Ω/square) were cleaned in ultrasonic bath with detergent, deionized water and ethanol for 10 min. Before film deposition, the FTO substrates were treated with ultraviolet ozone for 15 min. The NiO$_x$ films were prepared via a sol-gel method as described in the previous work[3]. The Ni(acac)$_2$ was dissolved in anhydrous ethanol (32.11 mg ml^{-1}) with the addition of 17 µl hydrochloric acid, and stirred overnight at room temperature. Prior to use, the solution was filtered through a 0.45 µm PTFE filter. The solution was spin coated on FTO substrates at 4,000 rpm for 40 s and annealed at 150 °C for 10 min. The entire deposition process was carried out in a dry box (≤30% RH). Then, the samples were transferred to a 180 °C preheating hotplate in ambient air (≤50% RH) for 10 min, followed by heating at 400 °C for 45 minutes. After annealing, the NiO$_x$ samples were transferred to the N$_2$ glovebox immediately for the subsequent interlayer deposition. Me-4PACz (1mg ml^{-1} in anhydrous ethanol; ultrasonic bath for 15 min) was spin coated at 3,000 rpm for 30 s, and annealed at 100°C for 10 min. We use 1.3 M $Cs_{0.05}FA_{0.9}PbI_3$ perovskites as the photoactive layers, and the precursor solutions were prepared by dissolving the 653.25 mg PbI_2, 12.99 mg CsI, and 212.38 mg FAI in a 1 mL mixed solvent (5:1 v:v) of DMF and DMSO, respectively. 0.97 mg MABr and 3.19 mg $PbBr_2$ and 9.79 mg MACl were additionally added into the precursor solution for better crystallization and perovskite phase transformation. The precursor solutions were stirred overnight at room temperature in a nitrogen-filled glovebox. The solutions were filtered with a 0.45 μm PTFE filter before use. The perovskite solutions were then spun on the substrates at 1,000 rpm. for 10 s and 4000 rpm. for 40 s. 150 μl of chlorobenzene (with or without 0.6mg ml^{-1} 2TI) was added dropwise onto the substrate 5 s before the end. The substrates were then placed on a pre-heated hotplate and annealed at 100 °C for 30 min. After cooling down, a mixture of 3F-PEAI (2 mg ml^{-1}) and MAI (1 mg ml^{-1}) was dissolved in IPA–DMF (200:1, v/v), spun onto the as-prepared perovskite films. Finally, C_{60} (20 nm), BCP (7 nm), and copper electrode (100 nm) were deposited sequentially using thermal evaporation under a high vacuum ($\leq 8\times10^{-5}$ Pa).

Device characterizations. The Fourier-transform infrared (FTIR) spectroscopy was obtained by using Thermo Fisher NICILET iS10. Nuclear magnetic resonance (NMR) characterization was characterized with a Bruker Avance NEO 600. The solvent in the NMR measurements is deuterated DMSO and the concentration of each solute in the solutions is 10 mg/ml. X-ray photoelectron spectroscopy (XPS) measurements were performed on a Thermo Fisher Scientific ESCALAB Xi+ instrument with a monochromatic Al K Alpha (1486.68 eV) X-ray source, and the samples were measured under an ultrahigh vacuum. The binding energies were calibrated using the C (1s) carbon peak (284.8 eV). All the high-resolution spectra were obtained under constant analyzer energy (CAE) mode with a pass energy of 30 eV and step size of 0.05 eV. X-ray diffraction (XRD) patterns were carried out by a Rigaku Smart lab 3 kW XRD (Rigaku Ltd., Japan) using Cu K_α radiation (λ = 0.15405 nm). The surface morphology of the samples was obtained using a scanning electron microscope (Gemini SEM 500, Zeiss). EQE spectra were measured using a Zolix-SCS600 system, calibrated by a calibrated crystalline Si reference cell. The custom-made in situ PL testing setup is positioned next to a hot plate, with an excitation laser (640 nm) being directed onto the sample through a fiber optic. During the annealing process of the perovskite, the PL spectral signals are collected every 20 ms by a detector connected to the spectrometer (TE-Cooled Micro Spectrometer, ATP5020R, Optosky Optical Ltd.). The *J-V* curves were measured (2400 Series Source Meter, Keithley Instruments) in the air under simulated AM 1.5G sunlight at 100 mW/cm^2 irradiation by a WACOM Class AAA (WXS-100S-5) simulator, with the intensity calibrated with a Fraunhofer ISE-calibrated silicon reference cell with KG1 filter. The mismatch factor was calculated to be less than 1% and applied to calibrate the AM 1.5 G 100 mW cm^{-2} equivalent irradiance. The active area of the solar cell measured under AM 1.5 G is 0.07 cm^2, defined by an opaque aperture mask. The *J–V* curves were measured at a scan rate of 200 mVs^{-1} (with no preconditioning) in ambient air (~25 ^{o}C and relative humidity ~ 50 %). For stabilized output measurements at the MPP, the device testing chamber was left under ambient conditions. Solar cells were measured at the MPP voltage, (determined from *J–V* sweeps in reverse scans) and the current output was tracked over time. For TRPL mapping measurement, a laser scanning confocal microscope system equipped 405nm laser (1 MHz, 3.1 µJ cm^{-2} per pulse) and galvo-based scanner was used in air. The objective was 100X with numerical aperture of 0.95. The lifetimes were collected based on time-correlated single photon counting (TCSPC), the resolution was set to 7ps with 4096 channels, The diameter of signal collection area for each sample was 20×20 um^2.

Density-functional theory (DFT) calculation

The Vienna Ab initio Simulation Package (VASP) was used for theoretical calculations based on the density functional theory (DFT). The electron-ion potential and exchange-correlation functional were described by projected augmented wave (PAW) and generalized gradient approximation (GGA)[4,5], respectively. The kinetic energy cutoff was set to 500 eV for the relaxation of geometric structures. A 5×5×5 Monkhorst-Pack *k*-point mesh was used in the Brillouin zone[6]. To avoid the periodic interaction, a vacuum region of 20 Å was used to avoid the periodic interaction. The stress force and energy convergence criterions are chosen as 0.01 eV/Å and 10^{-5} eV, respectively. To treat the van der Waals interaction between perovskites and organic molecules, a semi-empirical DFT-D2 method was employed[7]. The uniaxial strain applied to the perovskites is $\varepsilon = (a - a_0)/a_0 \times 100\%$, where a and a_0 are the strained and unstrained lattice constants.

Device simulation. Simulations of PSCs were conducted using the heterojunction solar cell simulator SCAPS-1D, version 3.3.11.

Long-term stability tests. The perovskite devices were encapsulated with ultraviolet adhesive (LT-U001, Lumtec) and a glass coverslip as a barrier layer in a nitrogen-filled glovebox. Before encapsulation, we blew the devices with a nitrogen gun to remove contamination and stored them in a nitrogen-filled glovebox for overnight to remove any residual moisture. We use a UV-containing large-area LED array as the light source. We do not have control over the humidity but monitored the laboratory humidity, which is around a relative humidity of ~ 50%, during the aging. For the MPP tracking, as the V_{MPP} may change over time, we have applied perturb-and-observe algorithms that carry out a periodic perturbation of the operating voltage maximizing the total power output of the device.

Note S1. Discussion on crystallization kinetics

Based on the evolution of PL peak positions and intensities, we assume the crystallization process of the perovskite film to occur in four stages:

Stage I: Rapid Nucleation. In this stage, the PL intensity increases along with a blue shift in the peak position, transitioning from 788 nm to 772 nm. Previous study revealed that during thermal annealing process, there exists a correlation between the peak position and grain size, where smaller grains lead to shorter emission wavelengths[8]. Therefore, we posit that the blue shift is attributed to the formation of numerous crystalline nuclei at the liquid-gas interface. These nuclei are smaller than those formed during the anti-solvent quenching process, a consequence of surface solvent evaporation driven by the temperature increase in the perovskite wet film[9]. Moreover, as illustrated by the dashed lines in Fig. 1e, g in the main text, the target film reaches the first maximum intensity faster than the control film by 20 ms, implying a faster nucleation rate that is advantageous for the subsequent crystallization. However, given that our in situ PL test involves data collection at 20 ms intervals, we consider this slight difference to be negligible. In summary, there are no significant differences between the two films in this stage.

Stage II: Crystallization-Dissolution Dynamic Equilibrium. In this stage, both PL intensity and peak position exhibit relatively stable behaviors. This stage involves a competition between the continued growth of crystalline nuclei in the upper wet perovskite film and the dissolution of the upper crystalline part due to the solvent evaporation of the lower part solution[10]. The former process enhances PL intensity, whereas the latter one leads to a decrease. As the solvent evaporation from the lower part slows down over time, the growing upper crystalline nuclei may hinder the evaporation of the lower solution, resulting in even slower evaporation of the lower solvent. Therefore, initially, there is a slight decrease in PL intensity, suggesting a faster dissolution process due to rapid evaporation of solution at lower part, followed by the opposite scenario. In the control film, PL intensity changes smoothly, indicating a linear progression of the process, with the crystallization process continuously favoring the growth of the crystalline nuclei. Rapid growth of the upper perovskite crystalline nuclei forming a shell-like structure can lead to many residual solvents in the lower part of the perovskite film, deteriorating the crystallization process and causing lattice distortion or even void formation[11]. In contrast, in the target film, the change in PL intensity is not as smooth, with fluctuations, similar to previous reports, leading to a significant extension of the second stage by 200 ms compared to the control film. As the competitive mechanism previously mentioned, we can reasonably speculate that with the addition of 2TI, the crystallization process in the second stage is modulated, restricting the growth of the upper wet film crystalline nuclei, widening the window for the evaporation of the lower part solvent, reducing solvent residue, and improving the crystallization of the lower part.

Notably, the PL peak position remains essentially unchanged during this stage, suggesting that the grain size does not change, and the PL intensity at the end of the second stage is close to that at the end of the first stage, implying the existence of this dynamic equilibrium process.

Stage III: Crystalline Nuclei Grow and Enlarge. In this stage, there is a rapid rise in PL peak intensity accompanied by a continual red shift in the peak position, signifying the ongoing enlargement of crystalline nuclei and the free growth of perovskite crystals in three dimensions, forming larger crystal structures[12,13]. The control group reaches its peak PL intensity at 600 ms, whereas the target group peaks at 800 ms. The 200 ms difference is attributed to the delay induced by the addition of 2TI in the second stage. Overall, there are no substantial differences between control and target films in this stage.

Stage IV: Crystal Aggregation. In this stage, PL intensity decreases and the peak position continues to redshift for a short duration before stabilizing. PL decrease is attributed to the upper perovskite crystals growing large enough to aggregate and form grain boundaries, a key source of non-radiative recombination in the film[8]. Consequently, the perovskite only continues to grow vertically, leading to the observed continued redshift of the PL peak.

Note S2. Details of simulation

We use device simulation techniques to analyze the impact of different ΔE on device performance. All our simulations of PSCs are conducted in Solar Cell Capacitance Simulator One dimension (SCAPS-1D), version 3.3.11[14]. AM 1.5 solar spectrum (100 mW/cm^2) is adopted for sunlight incidence. This software is mainly based on three differential equations (equation 1~equation 3) to give the simulation results.

$$\frac{\partial}{\partial x}\left(\varepsilon_0\varepsilon\frac{\partial\Psi}{\partial x}\right) = -q\left(p - n + N_D^+ - N_A^- + N_{def}\right) \quad (1)$$

$$-\frac{\partial J_n}{\partial x} - U_n + G = \frac{\partial n}{\partial x} \qquad (2)$$

$$-\frac{\partial J_p}{\partial x} - U_p + G = \frac{\partial p}{\partial x} \qquad (3)$$

Here, ε_0 is the Vacuum Permittivity, ε is the relative permittivity, Ψ is the electrostatic potential, q is the elementary charge, $n(p)$ is the electron (hole) density, $N_D^+\left(N_A^-\right)$ is the density of ionized donors (acceptors), N_{def} is the possible defect density, $J_n(J_p)$ is the electron (hole) current densities, $U_n(U_p)$ is the net electron (hole) recombination rate, G is the electron-hole generation rate. The electron and hole density are given by:

$$J_n = qn\mu_nE + qD_n\frac{\partial n}{\partial x} \qquad (4)$$

$$J_p = qp\mu_pE - qD_p\frac{\partial p}{\partial x} \qquad (5)$$

Where $\mu_n(\mu_p)$ is the electron (hole) mobility, and $D_n(D_p)$ is the diffusion coefficient of the electron (hole).

Typically, perovskite is considered as intrinsic semiconductor, and its Fermi level (E_f) can be calculated using the following formula:

$$E_f = \frac{E_C + E_V}{2} + \frac{1}{2}kTln\left(\frac{N_V}{N_C}\right) = \frac{E_C + E_V}{2} + \frac{3}{4}kTln\left(\frac{m_p^*}{m_n^*}\right)(6)$$

. where E_c is energy level of conduction band, E_v is energy level of valence band, k is Boltzmann's constant, T is temperature, N_c is the effective density of states for the conduction bands, N_v is the effective density of states for valence bands, $m_n^*(m_p^*)$ is electron(hole) effective mass. Therefore, we can alter the E_f of perovskite by adjusting the effective density of states ratio between the valence band and the conduction band in SCAPS-1D. In order to simulate the different Fermi level of the top and bottom surfaces of perovskite film, we set the band structure of the entire perovskite film to have a gradient variation in this simulation (near the HTL side, it is pure A, near the ETL side, it is pure B, with a linear distribution in between). It's worth noting that according to Equation 6, the ratio of N_c to N_v needs to follow a logarithmic distribution to fulfill the gradient distribution of the overall band structure.

To simplify the simulation process, we fix the value of E_c, E_v and N_v at the top and bottom parts of the perovskite to the same value, respectively. Subsequently, $E_{f,\text{ bottom}}$ can be adjusted by tuning the N_c value at bottom part of perovskite (pure A). The calculation formula for ΔE using the parameters included in SCAPS-1D is as follows:

$$\Delta E = E_{f,\text{ bottom}} - E_{f,\text{ top}}$$

$$= \left(\frac{E_C + E_V}{2} + \frac{1}{2}kTln\left(\frac{N_V}{N_C}\right)\right)_{\text{bottom}} - \left(\frac{E_C + E_V}{2} + \frac{1}{2}kTln\left(\frac{N_V}{N_C}\right)\right)_{\text{top}}$$

$$= \frac{1}{2}kTln\left(\frac{N_{v,bottom}}{N_{c,bottom}} * \frac{N_{c,top}}{N_{v,top}}\right) = \frac{3}{4}kTln\left(\frac{m_{p,bottom}^*}{m_{n,bottom}^*} / \frac{m_{p,top}^*}{m_{n,top}^*}\right)$$

$$= \frac{1}{2}kTln\left(\frac{N_{c,top}}{N_{c,bottom}}\right) \qquad (7)$$

Integrating Equations 6 and 7, it becomes evident that the value of ΔE is correlated with the ratio of the effective masses of electrons and holes at the top and bottom surfaces, prompting the discussion in Section 2 of our text.

The relevant simulation parameters are listed in Table S2 and 3.

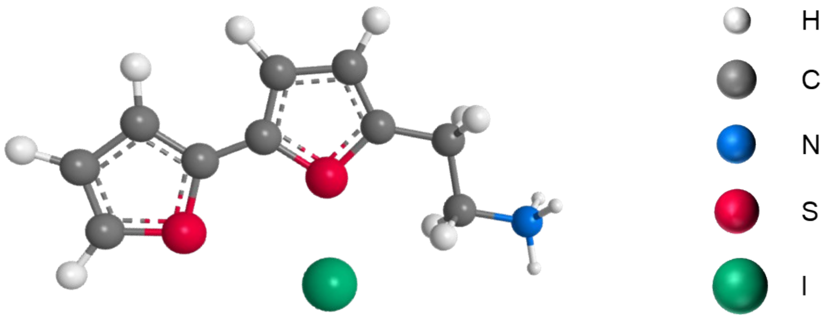

2TI

Fig. S1 Molecular structure of 2TI.

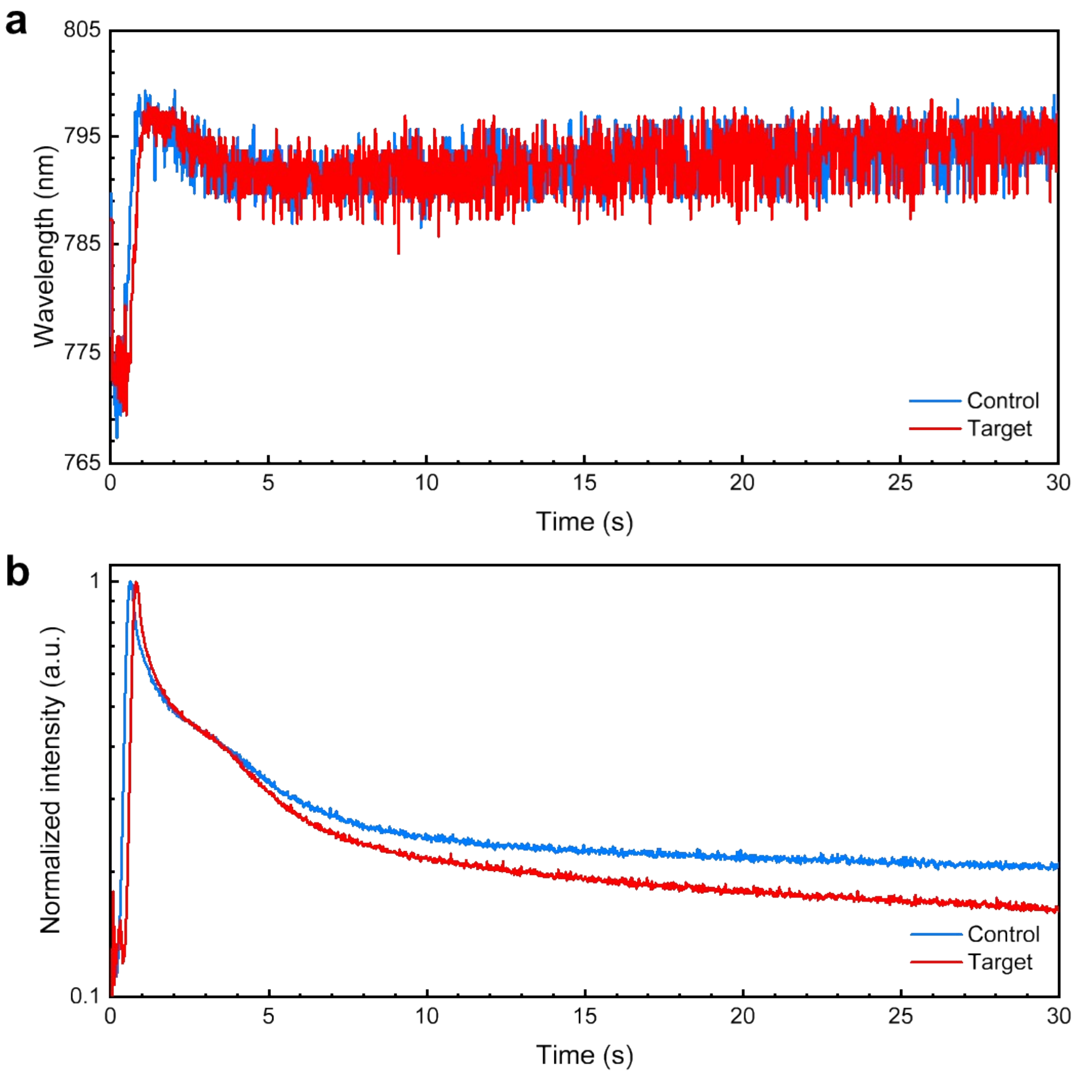

Fig. S2 The extracted values of **(a)** emission peak position and **(b)** normalized PL peak intensity of control and target films in a long-time scale. In a long-time scale, the shifts in peak positions are nearly identical for both. However, it can be observed that the peak intensity in the target film decreases more rapidly compared to the control film.

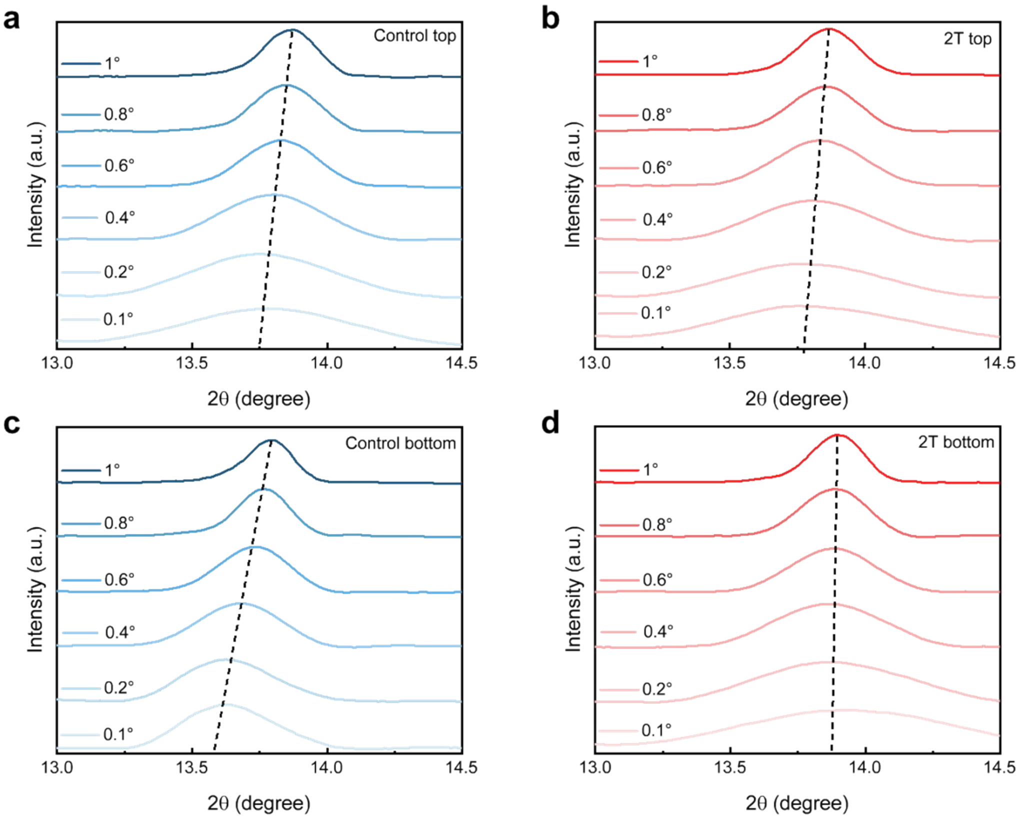

Fig. S3 GIXRD spectrum of the top surface of control **(a)** and target **(b)** films, and the bottom surface of control **(c)** and target **(d)** films. The dashed lines represent the peak shifts.

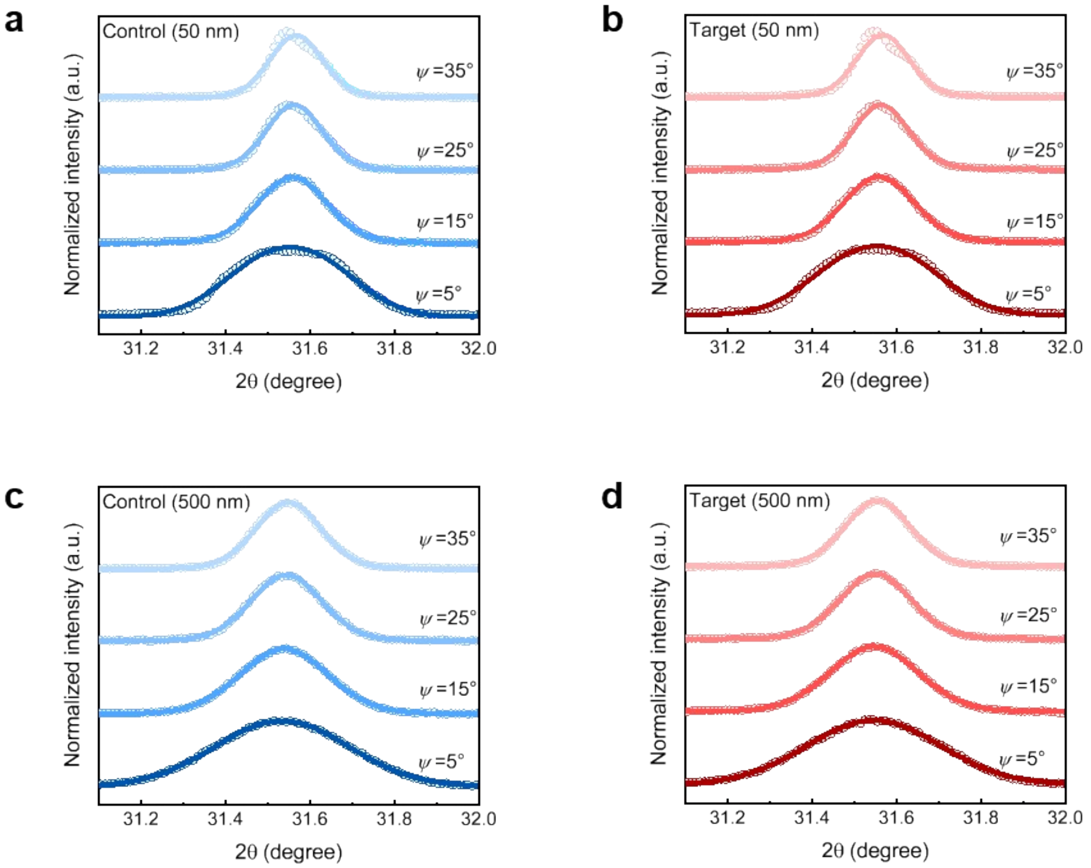

Fig. S4 GIXRD spectrum of wide-bandgap perovskite at different tilt angles at the depth of 50 nm for control **(a)** and target **(b)** films and 500 nm for control **(c)** and target **(d)** films.

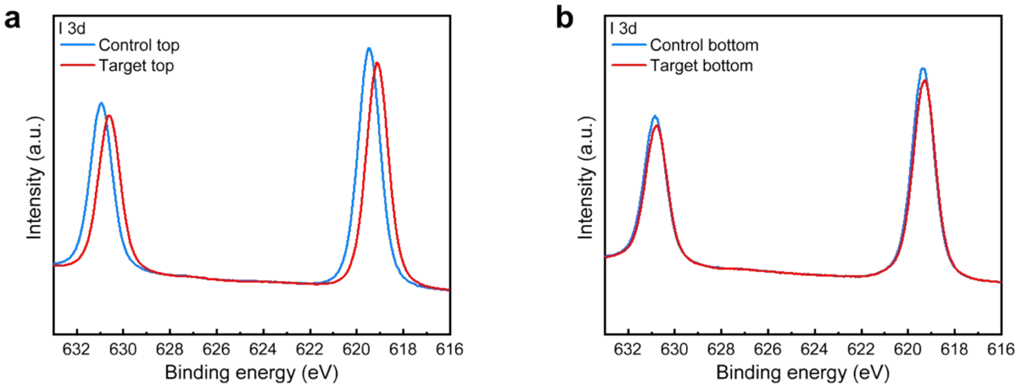

Fig. S5 I 3d XPS spectra of **(a)** the top and **(b)** bottom surface of control and target films.

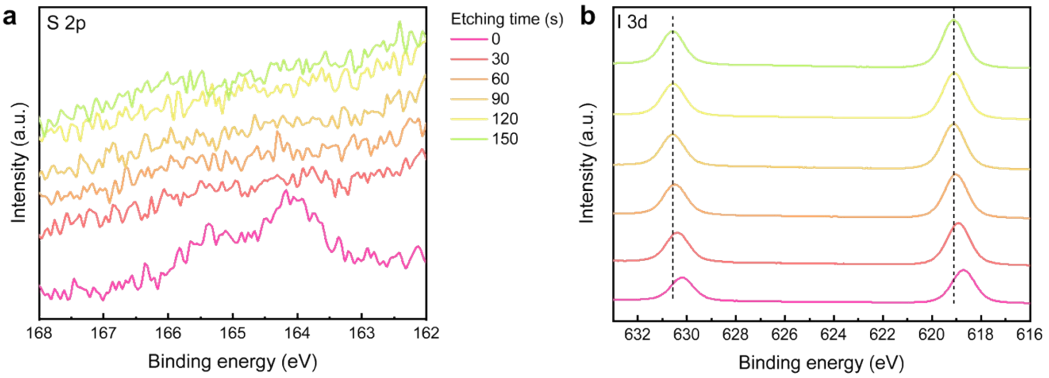

Fig. S6 XPS depth profile analysis of S 2p **(a)** and I 3d **(b)** for perovskite films with the addition of 2TI.

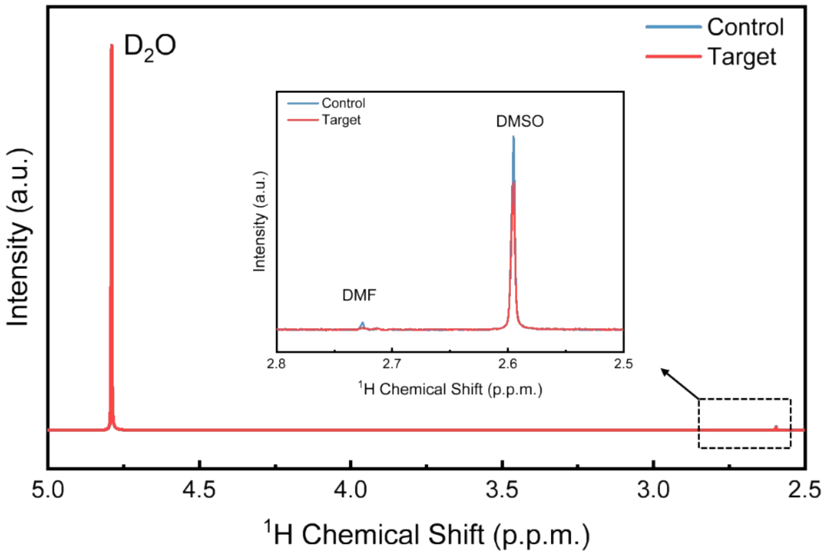

Fig. S7 The 1H NMR spectra of control and target perovskite films dispersed in D_2O. We observe reduction in peak densities of both the DMF and DMSO signals[15,16], indicating less solvent residue upon 2TI treatment.

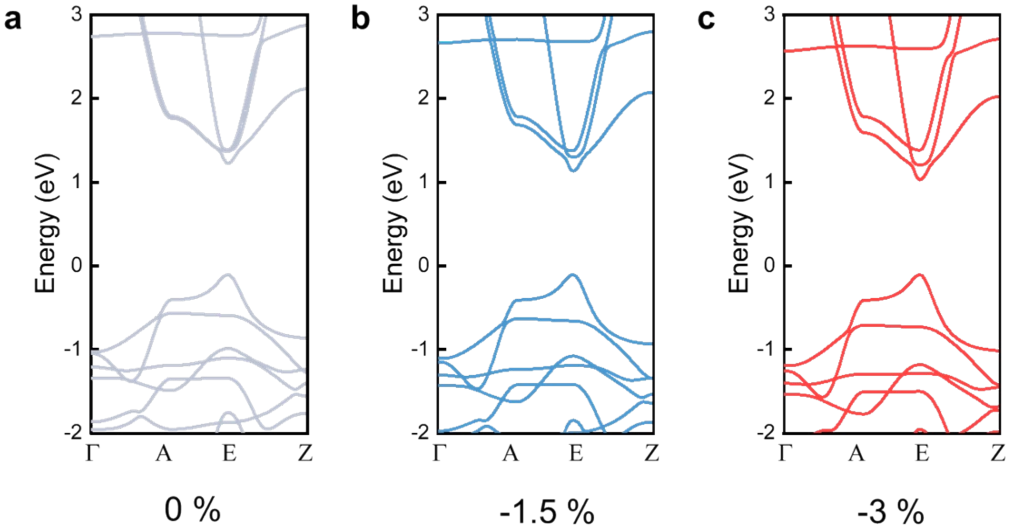

Fig. S8 Band structures under different strain conditions based on first-principles density functional theory. We present three typical cases herein: strain = **(a)** 0%, **(b)** -1.5%, **(c)** -3%.

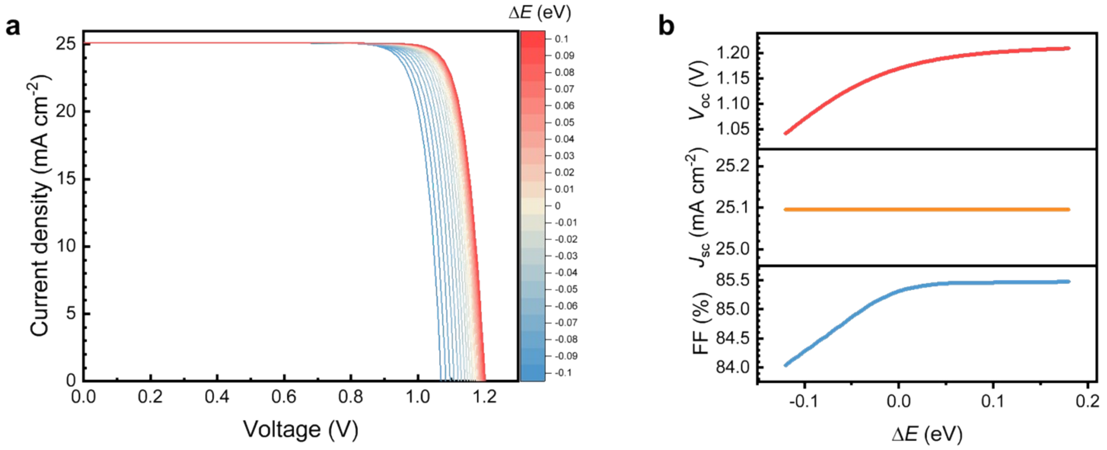

Fig. S9 (a) Simulated *J*–*V* curves of devices with different representative ΔE. **(b)** Dependence of the V_{oc}, J_{sc} and FF on ΔE.

Note S3. Further discussion about the impact of Δ*E* on charge transport.

In Fig. S10, we schematically depict the ideal scenario for charge transport within a perovskite photo absorber, where the holes and electrons preferentially diffuse towards HTL and ETL, respectively. When $\Delta E < 0$ eV, after photoexcitation, the electrons tend to diffuse towards the side with low Fermi energy to occupy empty energy states, as illustrated in the schematic diagram shown in Fig. S10b. This results in electron accumulation near the HTL interface, aligning the electron distribution trends with those of hole, leading to a reduction in the hole-to-electron ratio as it approaches the ETL (Fig. S10b). This scenario would be unfavorable for the device operation in inverted cell architecture. When $\Delta E = 0$ eV, holes and electrons are more uniformly distributed within the perovskite film due to the absence of energy landscape differences (Fig. S10c). When $\Delta E > 0$ eV, electrons tend to flow towards the ETL side driven by the low Fermi energy near this region, resulting in preferential electron accumulation at the ETL side (Fig. S10d). Meanwhile, the holes tend to diffuse towards the side with high Fermi level (*i.e.* the HTL side), resulting in a high hole-to-electron ratio at this interface. This scenario would be highly favourable for device operational devices. Furthermore, we also investigated the band structure under ΔE. It is evident that with the improvement (i.e., increase) of ΔE within the perovskite thin films, the quasi-Fermi level correspondingly rises.

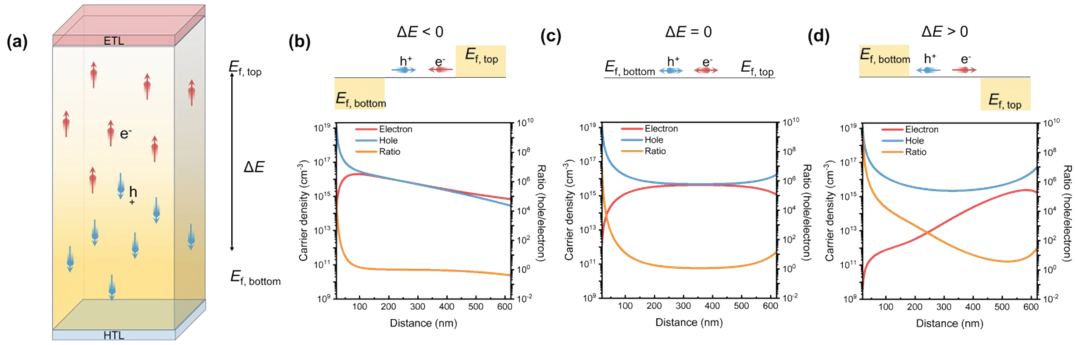

Fig. S10 Simulation analysis of different energy band landscapes on device performance. **(a)** Schematic diagrams illustrating charge transport within perovskite photo absorber in an inverted cell. The ETL and HTL stand for electron-transporting layer and hole-transporting layer, respectively. The $E_{f,\text{ top}}$ and $E_{f,\text{ bottom}}$ represent the Fermi level of the top (close to ETL) and bottom (close to HTL) region of the perovskite film. The ΔE is defined as the $E_{f,\text{ bottom}}$ subtracted by the $E_{f,\text{ top}}$. The blue and red circles depicit photogenerated holes (h^+) and electrons (e^-), respectively. **(b)** – **(d)** Charge transport and distribution of hole and electron concentrations and the ratio of hole to electron of the three different ΔE scenarios: **(b)** > 0, **(c)** = 0, **(d)** < 0.

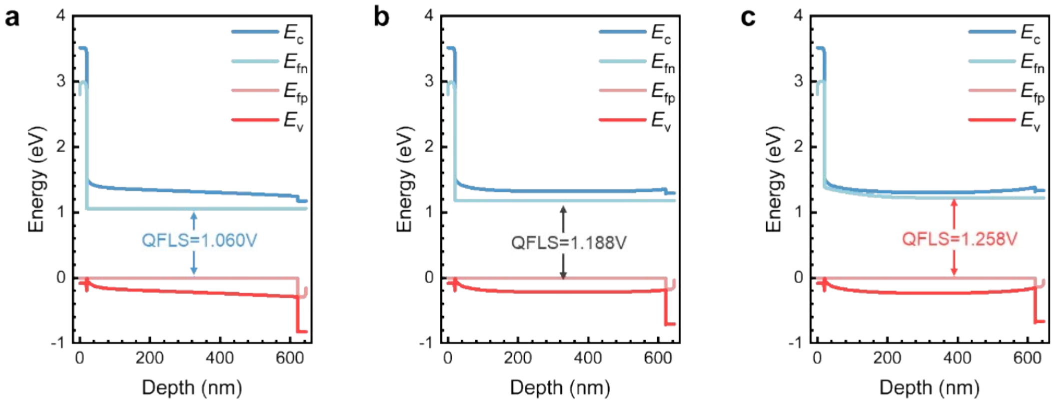

Fig. S11 The simulated band diagram of three different Δ*E* scenarios: **(a)** > 0, **(b)** = 0, **(c)** < 0.

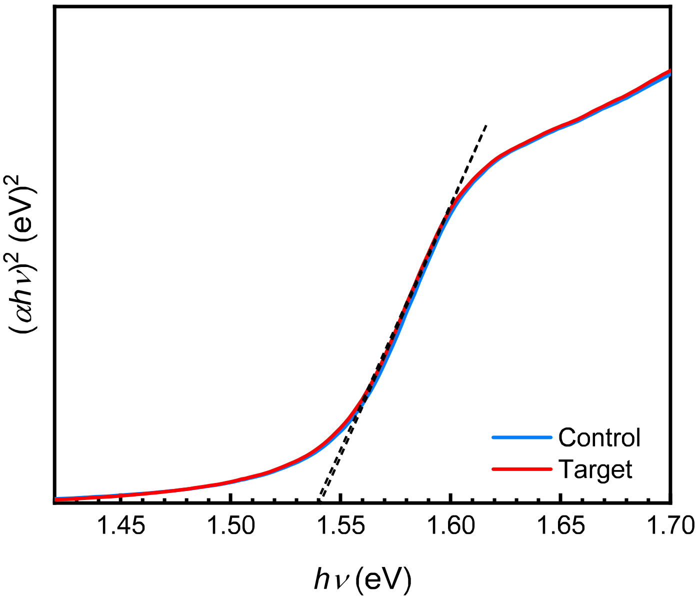

Fig. S12 Tauc plots of absorption spectra of control and target films. The extracted E_g values are 1.54 eV.

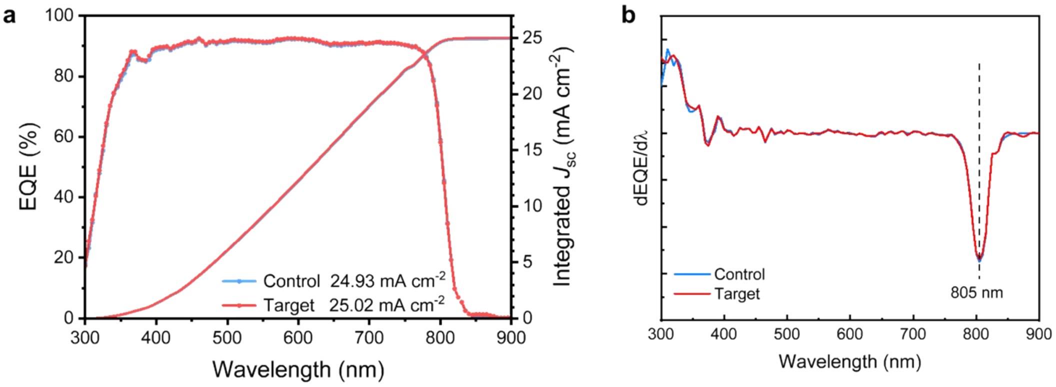

Fig. S13 (**a**) EQE spectrum and integrated J_{sc} of control and target device. The measured J_{sc} values from J-V analysis is consistent with the integrated J_{sc} values from the EQE analysis with only exhibit less than 1.9% mismatch. (**b**) Inflection points of EQE. The inflection points of the control and target perovskite are both at 805nm, and the obtained bandgap value is 1.54 eV, which is consistent with the results obtained by Tauc plot.

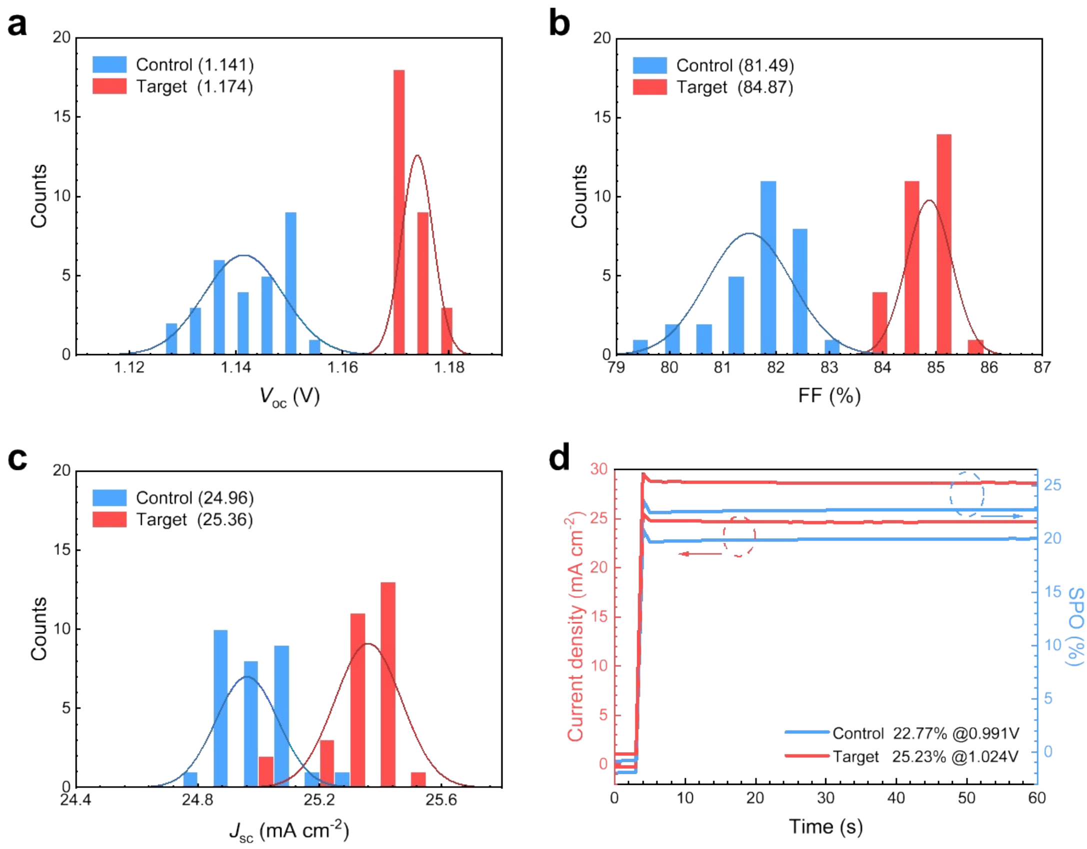

Fig. S14 Histograms showing the device **(a)** V_{oc}, **(b)** FF and **(c)** J_{sc} of 30 cells per type, fitted with Gaussian distributions (solid lines). The values in parentheses represent the average values. **(d)** Stable power output (SPO) of the best-performing control and target devices.

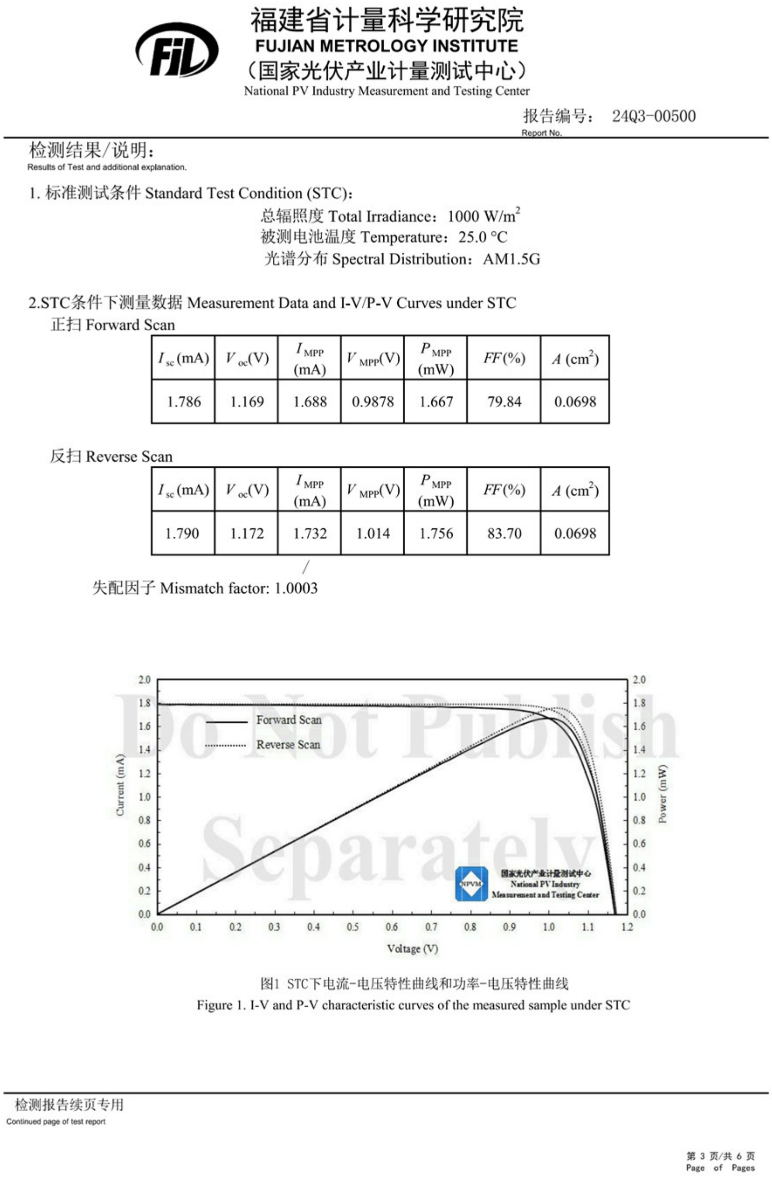

福建省计量科学研究院
FUJIAN METROLOGY INSTITUTE
（国家光伏产业计量测试中心）
National PV Industry Measurement and Testing Center

报告编号： 24Q3-00500
Report No.

检测结果/说明：
Results of Test and additional explanation.

1. 标准测试条件 Standard Test Condition (STC)：
总辐照度 Total Irradiance：1000 W/m^2
被测电池温度 Temperature：25.0 °C
光谱分布 Spectral Distribution：AM1.5G

2.STC条件下测量数据 Measurement Data and I-V/P-V Curves under STC

正扫 Forward Scan

I_{sc} (mA)	V_{oc}(V)	I_{MPP} (mA)	V_{MPP}(V)	P_{MPP} (mW)	FF(%)	A (cm^2)
1.786	1.169	1.688	0.9878	1.667	79.84	0.0698

反扫 Reverse Scan

I_{sc} (mA)	V_{oc}(V)	I_{MPP} (mA)	V_{MPP}(V)	P_{MPP} (mW)	FF(%)	A (cm^2)
1.790	1.172	1.732	1.014	1.756	83.70	0.0698

/

失配因子 Mismatch factor: 1.0003

图1 STC下电流-电压特性曲线和功率-电压特性曲线
Figure 1. I-V and P-V characteristic curves of the measured sample under STC

检测报告续页专用
Continued page of test report

第 3 页/共 6 页
Page of Pages

Fig. S15 Certification report of the 0.0698-cm^2 cells tested by the Chinese National PV Industry Measurement and Testing Center (NPVM), showing the I-V and P-V characteristic curves measured under standard test condition (STC).

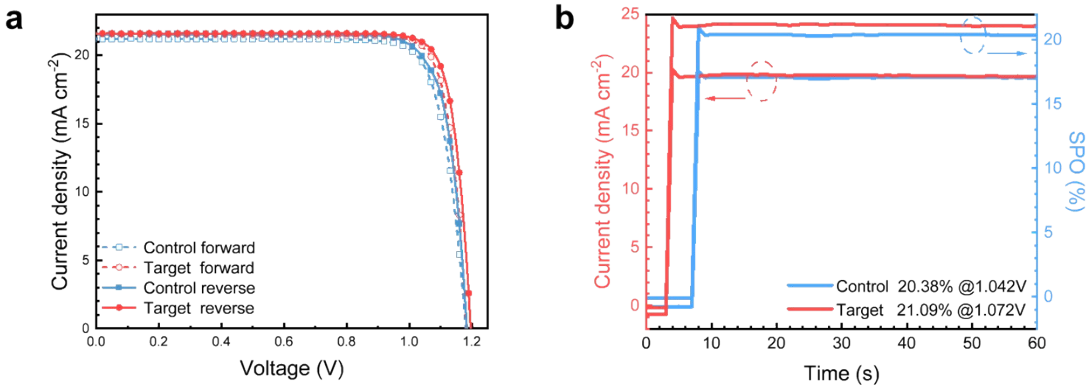

Fig. S16 (a) *J*-*V* curves of the best-performing control (blue) and target (red) devices of wide-bandgap perovskite solar cell. The devices are scanned in both reverse (solid lines) and forward (dashed lines) directions. **(b)** SPO of control and target devices.

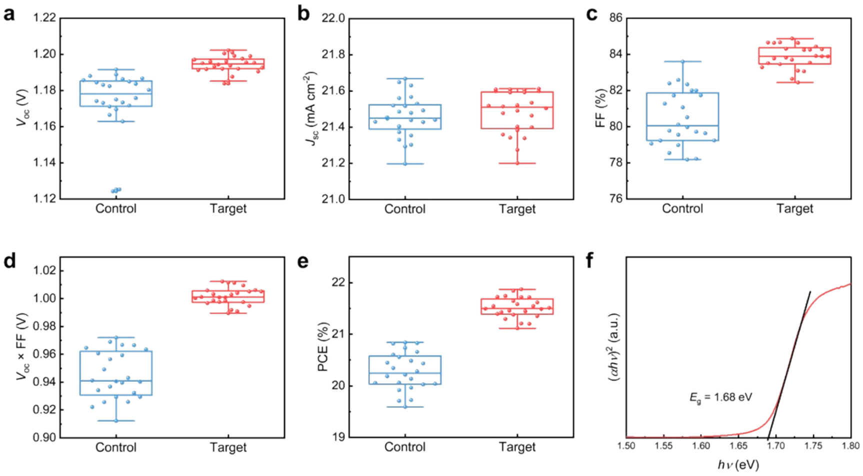

Fig. S17 Histograms showing the device **(a)** V_{oc}, **(b)** J_{sc}, **(c)**FF, **(d)**V_{oc}×FF and **(e)**PCE of 24 cells per type, fitted with Gaussian distributions (solid lines). **(f)** Tauc plots of absorption spectra of wide-bandgap perovskite films. The extracted E_g values are 1.68 eV.

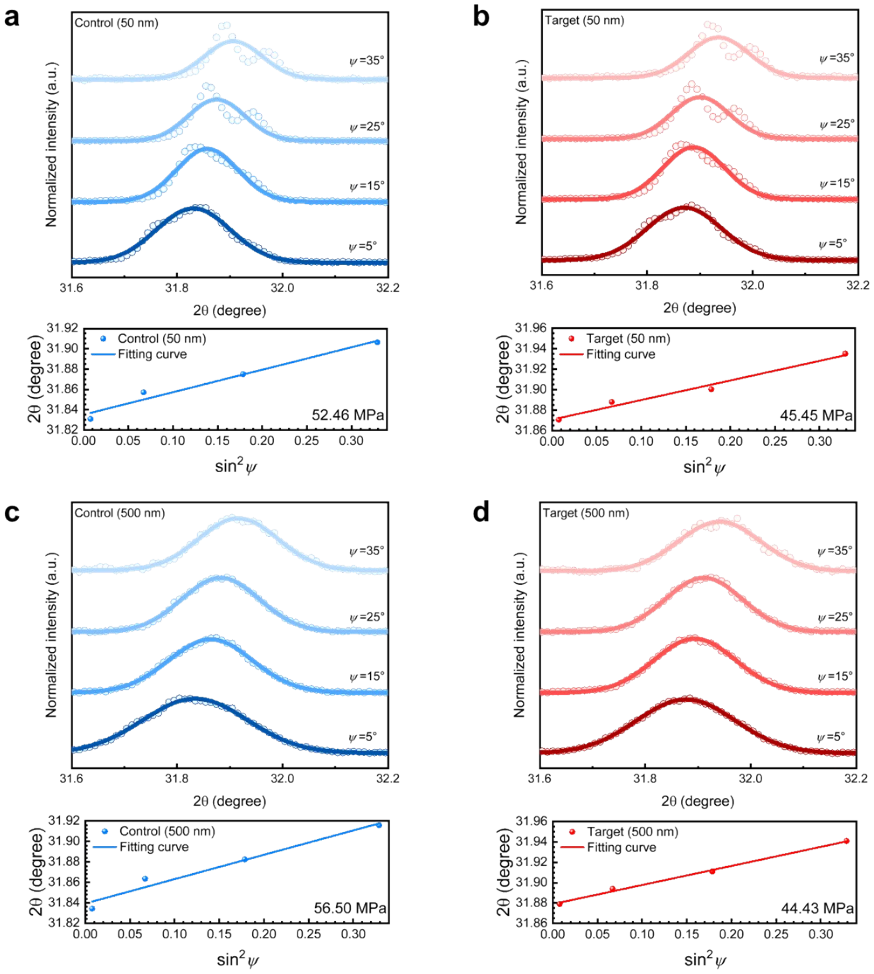

Fig. S18 GIXRD spectrum of wide-bandgap perovskite at different tilt angles at the depth of 50 nm for control **(a)** and target **(b)** films and 500 nm for control **(c)** and target **(d)** films. Bottom: strain distribution for the films (measured (points) and Gauss fitted (line) diffraction strain data as a function of sin$^{2}\varphi$).

Note S4. Experimental procedures of vertical charge transport

Inspired by previous work, we utilize transient PL spectroscopy with emission wavelength resolution to investigate charge transport behavior in the vertical direction. The transient PL spectroscopy is recorded with a time-correlated single photon counter (PicoQuant GmbH, TimeHarp 260) equipped with a monochromator (Omni λ3008i, the wavelength resolution is 0.1 nm), excited with a picosecond diode laser (640 nm, LDH-P-C-640B) at a repetition rate of 1 MHz. The laser excitation fluence is 3.2 nJ cm^{-2}. We use the monochromator to perform single time-resolved photoluminescence (TRPL) tests on emission signals every 1 nm within the 765-845 nm range, with each test having an integration time of 100 seconds. The PL1 signal corresponds to the aggregated emission from 805 to 845 nm, whereas the PL2 signal corresponds to the aggregated emission from 765 to 805 nm.

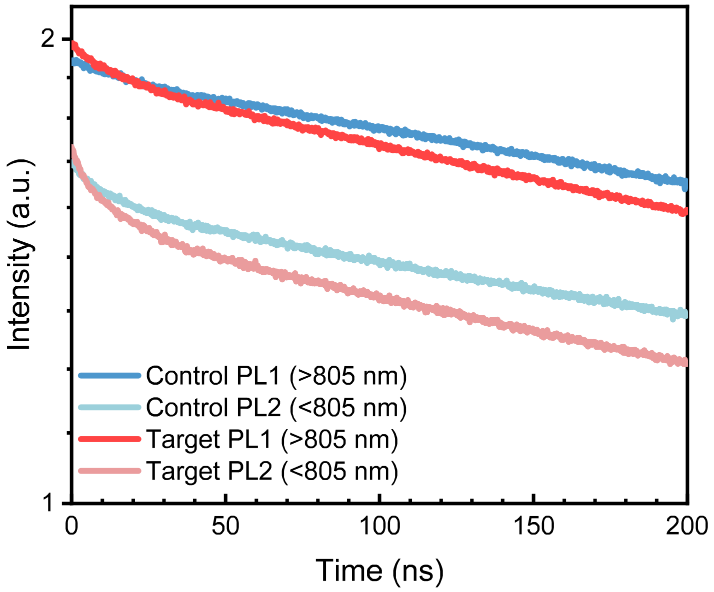

Fig. S19 Transient decay curve of the control and target films, collected at different wavelengths (PL1 > 805 nm and PL2 < 805 nm).

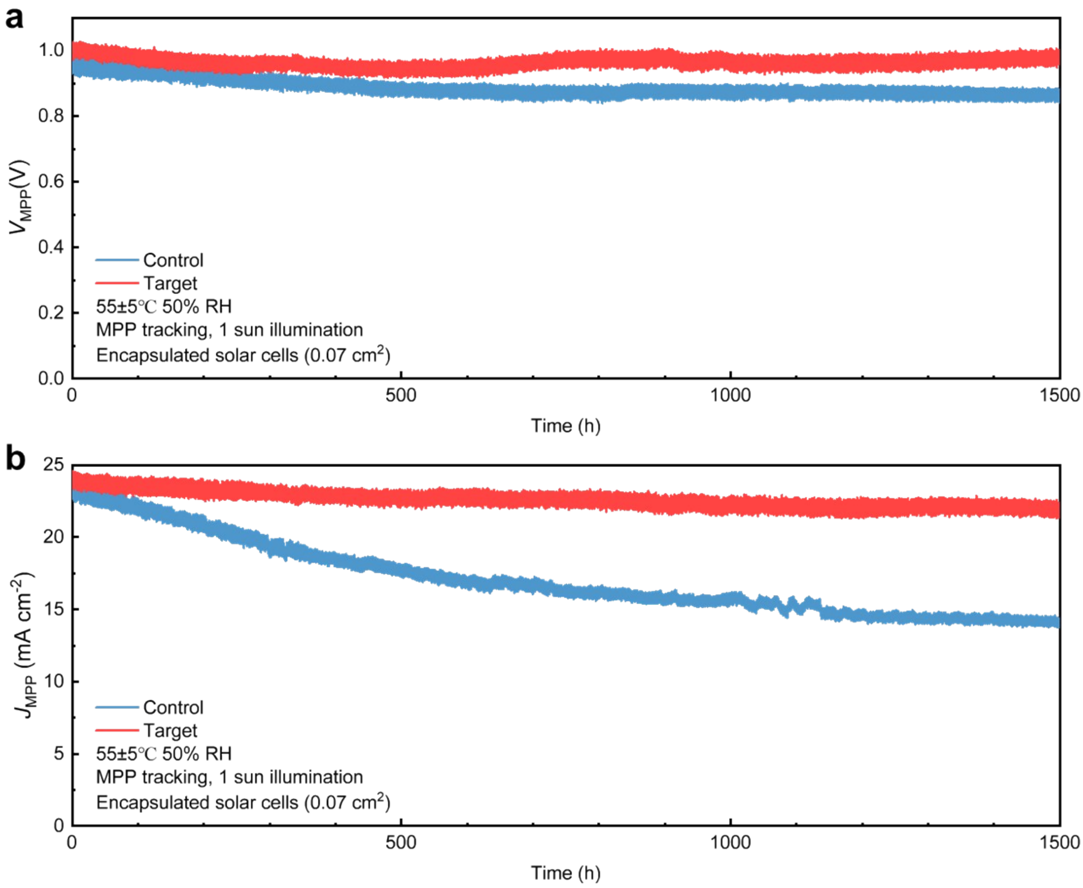

Fig. S20 The **(a)** V_{MPP} and **(b)** J_{MPP} of control and target devices in Fig. 5a.

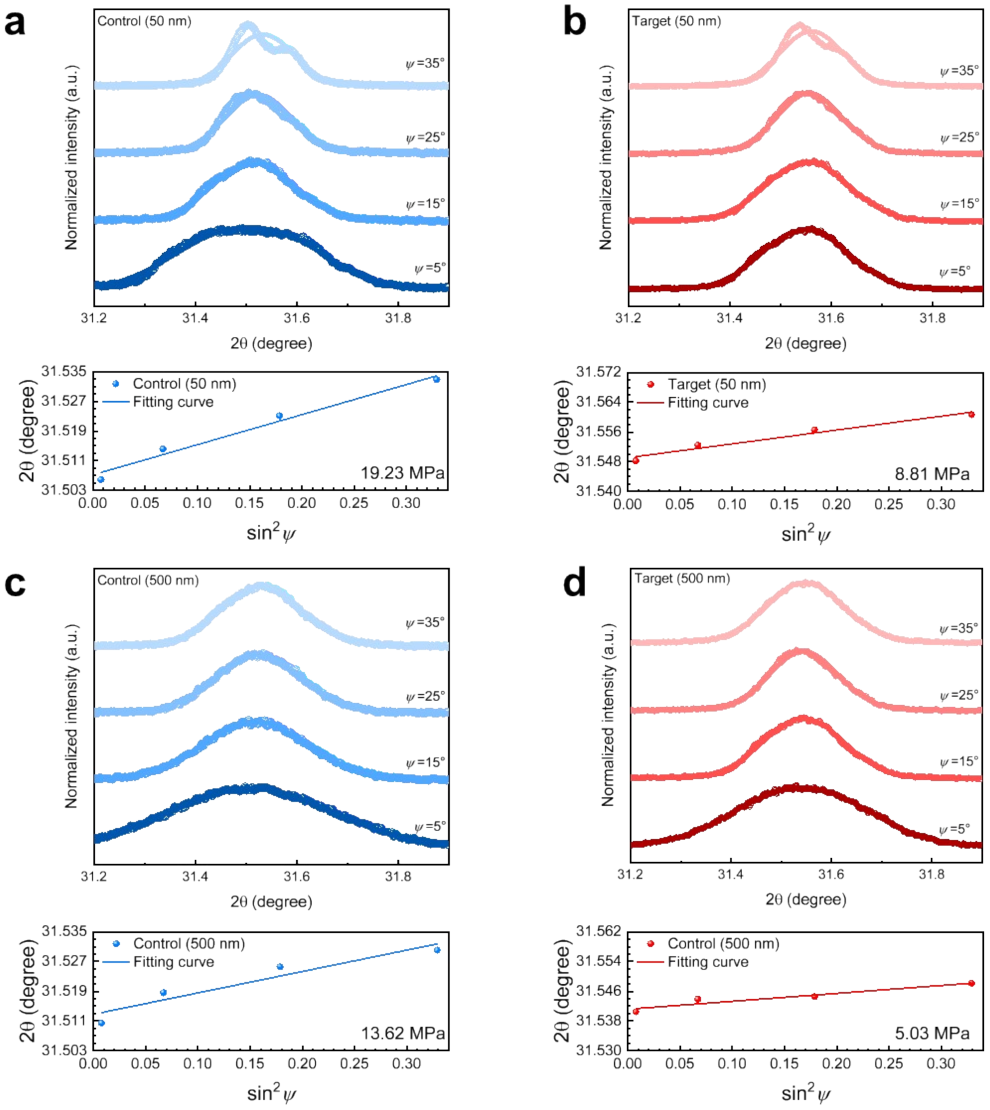

Fig. S21 GIXRD spectrum at different tilt angles at the depth of 50 nm for control (**a**) and target (**b**) films and 500 nm for control (**c**) and target (**d**) films after aging in ambient conditions. Bottom: strain distribution for the films (measured (points) and Gauss fitted (line) diffraction strain data as a function of $\sin^2\varphi$).

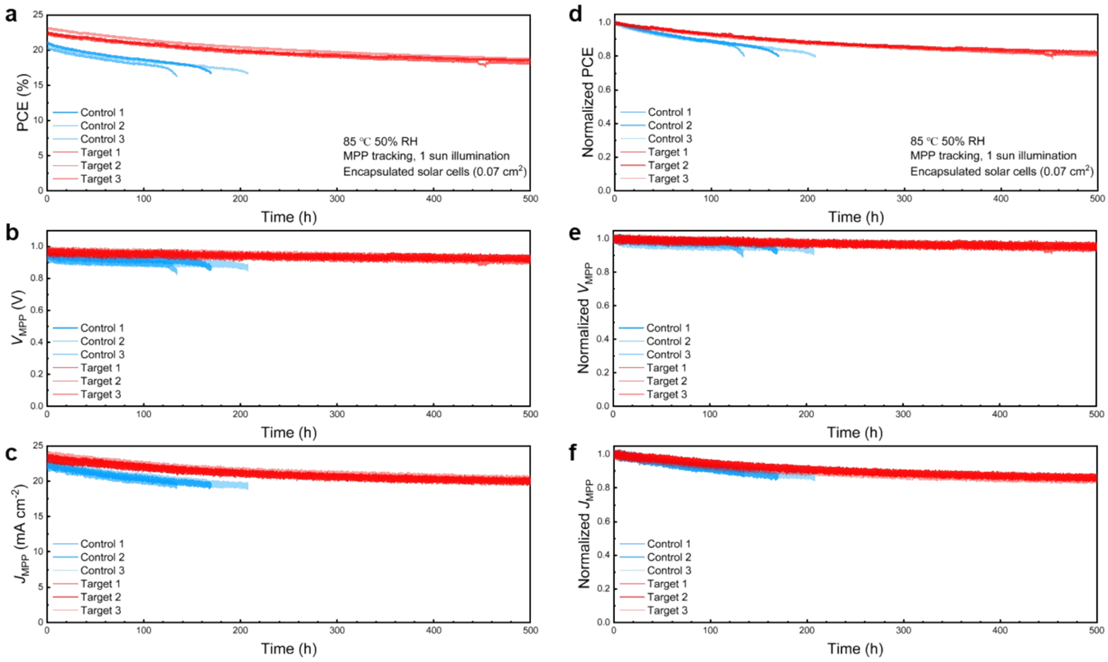

Fig. S22 (a) Long-term stability of the devices aged at 85 °C and 50% relative humidity under 1-sun equivalent illumination and the corresponding V_{MPP} **(b)** and J_{MPP} **(c)** evolution. **(d-f)** Corresponding normalized data for clearer observation of the performance evolution of the control and target device.

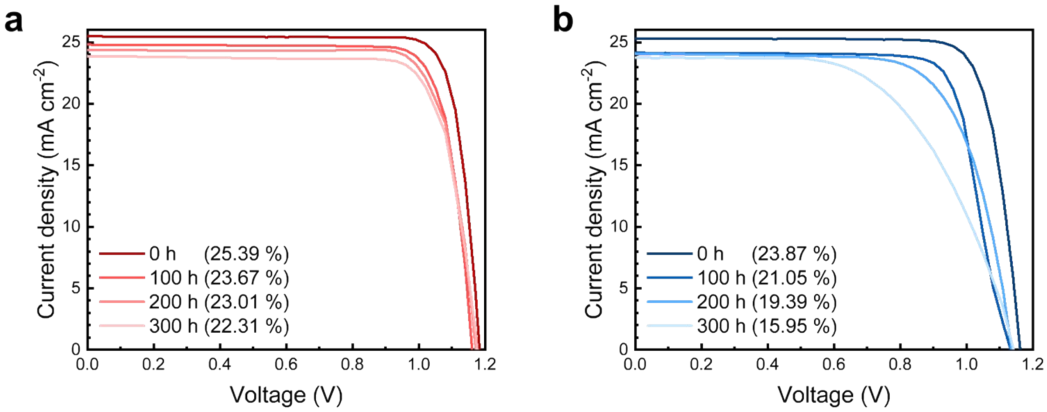

Fig. S23 Long-term stability of the **(a)** target and **(b)** control devices aged at 85 °C in the nitrogen glove box without illumination during 300 h.

Table S1. Instrumental angles (*Ψ*, *ω*, *Φ*) set for (012) crystal plane in different depths of GIXRD residual stress measurements.

Ψ (°)	50 nm		500 nm	
	ω (°)	*Φ* (°)	*ω* (°)	*Φ* (°)
5	0.3114	-17.5492	3.4807	-21.7563
15	0.3213	-43.0644	3.6065	-50.1414
25	0.3427	-56.8029	3.8835	-63.4648
35	0.3796	-64.3174	4.3772	-70.5945

Table S2. Relevant parameters used for simulation in SCAPS-1D. The relevant parameters are derived from reference literature[17–21].

Parameter	**HTL**	**Perovskite**		**ETL**
Thickness(nm)	20	680		25
Bandgap(eV)	3.6	1.54		2.2
Composition		A	B	
Electron affinity (eV)	2	3.88	3.88	3.87
Dielectric permittivity (relative)	11.75	30	30	4.2
CB effective density of states (cm^{-3})	2.5×10^{20}	Various	1×10^{18}	8×10^{19}
VB effective density of states (cm^{-3})	2.5×10^{20}	2.2×10^{19}	2.2×10^{19}	8×10^{19}
Electron/hole thermal velocity (cm/s)	1×10^{7}	1×10^{7}	1×10^{7}	1×10^{7}
Electron mobility (cm^2/Vs)	1×10^{-3}	10	10	20
Hole mobility (cm^2/Vs)	1×10^{-3}	10	10	1×10^{-2}
Shallow uniform donor density N_D (cm^{-3})	0	0	0	1×10^{18}
Shallow uniform acceptor density N_A (cm^{-3})	1×10^{19}	0	0	0

Table S3. Defect parameters used for simulation in SCAPS-1D.

Defect parameter	**HTL**	**HTL /Perovskite interface**	**Perovskite**	**ETL /Perovskite interface**	**ETL**
Defect type	Neutral	Neutral	Neutral	Neutral	Neutral
Capture cross section (electrons) (cm^{-3})	1×10^{-15}	1×10^{-19}	1×10^{-15}	1×10^{-19}	1×10^{-15}
Capture cross section (hole) (cm^{-3})	1×10^{-15}	1×10^{-19}	1×10^{-15}	1×10^{-19}	1×10^{-15}
Energetic distribution	Single	Single	Single	Single	Single
Energy level (eV)	0.6	0.6	0.6	0.6	0.6
Total defect density (cm^{-2})	1×10^{14}	1×10^{12}	1×10^{14}	1×10^{13}	1×10^{14}

Table S4. Performance parameters of the best device in in Fig. 4a in the main text.

Device		**V_{oc} (V)**	**J_{sc} (mA cm^{-2})**	**FF (%)**	**PCE (%)**
Control	Forward	1.125	24.81	81.40	22.72
	Reverse	1.147	25.23	82.78	23.96
Target	Forward	1.177	25.59	84.29	25.39
	Reverse	1.184	25.73	85.21	25.96

Table S5. Summary of reported state-of-the-art perovskite solar cell. R represents the V_{oc}×FF relative to the S-Q limits of its corresponding bandgap.

E_g (eV)	V_{oc} (V)	J_{sc} (mA/cm^2)	FF (%)	PCE (%)	V_{oc}*FF (V)	R (%)	Ref.
1.535	1.161	26.30	80.00	24.40	0.929	81.53	[22]
1.550	1.195	25.77	80.19	24.69	0.958	83.00	[23]
1.528	1.174	25.90	83.26	25.32	0.977	86.21	[24]
1.550	1.190	24.70	83.60	24.56	0.995	86.20	[25]
1.530	1.150	26.19	83.90	25.27	0.973	85.72	[26]
1.560	1.187	25.69	84.73	25.86	1.006	86.48	[27]
1.560	1.201	24.80	84.50	25.16	1.015	87.26	[28]
1.560	1.160	24.40	82.50	23.30	0.957	82.27	[29]
1.550	1.184	25.68	82.32	25.00	0.975	84.47	[30]
1.550	1.159	25.02	83.05	24.09	0.963	83.43	[31]
1.550	1.177	24.80	84.30	24.60	0.992	85.94	[32]
1.550	1.190	24.55	84.78	24.80	1.009	87.41	[13]
1.550	1.208	25.08	84.37	25.60	1.019	88.28	[33]
1.550	1.200	24.70	82.00	24.30	0.984	85.25	[34]
1.540	1.160	25.73	82.50	24.50	0.957	83.67	[35]
1.540	1.170	25.50	82.50	24.60	0.965	84.37	[36]
1.530	1.160	26.30	83.00	25.40	0.963	84.84	[37]
1.520	1.164	26.14	85.74	26.09	0.998	88.59	[38]
1.520	1.176	25.88	82.50	25.10	0.970	86.11	[39]
1.534	1.165	26.22	82.20	25.12	0.958	84.14	[40]
1.540	1.170	25.72	83.67	25.17	0.979	85.60	[41]
1.530	1.190	25.40	84.60	25.60	1.007	88.72	[42]
1.520	1.193	26.66	81.31	25.90	0.988	87.71	[43]
1.540	**1.191**	**25.49**	**85.14**	**25.85**	**1.014**	**88.69**	**This work**

Table S6. Performance parameters of the best device in in Fig. S16a.

Device		**V_{oc} (V)**	**J_{sc} (mA cm^{-2})**	**FF (%)**	**PCE (%)**
Control	Forward	1.180	21.20	81.73	20.45
	Reverse	1.183	21.56	81.72	20.84
Target	Forward	1.184	21.60	84.27	21.54
	Reverse	1.196	21.60	84.66	21.87

Supplementary Reference:

1 J. Y. Park, R. Song, J. Liang, L. Jin, K. Wang, S. Li, E. Shi, Y. Gao, M. Zeller, S. J. Teat, P. Guo, L. Huang, Y. S. Zhao, V. Blum and L. Dou, *Nat. Chem.*, 2023, **15**, 1745–1753.

2 E. Shi, B. Yuan, S. B. Shiring, Y. Gao, Akriti, Y. Guo, C. Su, M. Lai, P. Yang, J. Kong, B. M. Savoie, Y. Yu and L. Dou, *Nature*, 2020, **580**, 614–620.

3 Y. Yang, S. Cheng, X. Zhu, S. Li, Z. Zheng, K. Zhao, L. Ji, R. Li, Y. Liu, C. Liu, Q. Lin, N. Yan and Z. Wang, *Nat. Energy*, 2024, **9**, 37–46.

4 J. P. Perdew, K. Burke and M. Ernzerhof, *Phys. Rev. Lett.* , 1997, **78**, 1396.

5 P. E. Blöchl, *Phys. Rev. B*, 1994, **50**, 17953–17979.

6 H. J. Monkhorst and J. D. Pack, *Phys. Rev. B*, 1976, **13**, 5188–5192.

7 A.-R. Allouche, *J. Comput. Chem.*, 2011, **32**, 174–182.

8 V. Held, N. Mrkyvkova, P. Nádaždy, K. Vegso, A. Vlk, M. Ledinský, M. Jergel, A. Chumakov, S. V. Roth, F. Schreiber and P. Siffalovic, *J. Phys. Chem. Lett.*, 2022, **13**, 11905–11912.

9 Y. Wang, Z. Zeng, Y. Zhang, Z. Zhang, L. Bi, A. He, Y. Cheng, A. K. Y. Jen, J. C. Ho and S. W. Tsang, *Advanced Materials*, 2024, **36**, 2307635.

10 S. Wang, T. Yang, Y. Yang, Y. Du, W. Huang, L. Cheng, H. Li, P. Wang, Y. Wang, Y. Zhang, C. Ma, P. Liu, G. Zhao, Z. Ding, S. Liu and K. Zhao, *Adv. Mater.*, 2023, **35**, 2305314.

11 S. Chen, X. Dai, S. Xu, H. Jiao, L. Zhao and J. Huang, *Science*, 2021, **373**, 902–907.

12 L. Bi, Q. Fu, Z. Zeng, Y. Wang, F. R. Lin, Y. Cheng, H. L. Yip, S. W. Tsang and A. K. Y. Jen, *J. Am. Chem. Soc.*, 2023, **145**, 5920–5929.

13 F. Li, X. Deng, Z. Shi, S. Wu, Z. Zeng, D. Wang, Y. Li, F. Qi, Z. Zhang, Z. Yang, S. H. Jang, F. R. Lin, S. -W Tsang, X. K. Chen and A. K. Y. Jen, *Nat. Photon.*, 2023, **17**, 478–484.

14 A. Niemegeers and M. Burgelman, in *Conference Record of the Twenty Fifth IEEE Photovoltaic Specialists Conference - 1996*, 1996, pp. 901–904.

15 D. P. McMeekin, P. Holzhey, S. O. Fürer, S. P. Harvey, L. T. Schelhas, J. M. Ball, S. Mahesh, S. Seo, N. Hawkins, J. Lu, M. B. Johnston, J. J. Berry, U. Bach and H. J. Snaith, *Nat Mater*, 2023, **22**, 73–83.

16 H. E. Gottlieb, V. Kotlyar and A. Nudelman, *J Org Chem*, 1997, **62**, 7512–7515.

17 H. Chen, A. Maxwell, C. Li, S. Teale, B. Chen, T. Zhu, E. Ugur, G. Harrison, L. Grater, J. Wang, Z. Wang, L. Zeng, S. M. Park, L. Chen, P. Serles, R. A. Awni, B. Subedi, X. Zheng, C. Xiao, N. J. Podraza, T. Filleter, C. Liu, Y. Yang, J. M. Luther, S. De Wolf, M. G. Kanatzidis, Y. Yan and E. H. Sargent, *Nature* , 2022, **613**, 676–681.

18 L. Hao, T. Li, X. Ma, J. Wu, L. Qiao, X. Wu, G. Hou, H. Pei, X. Wang and X. Zhang, *Opt Quantum Electron*, 2021, **53**, 524.

19 G. Yang, Z. Ni, Z. J. Yu, B. W. Larson, Z. Yu, B. Chen, A. Alasfour, X. Xiao, J. M. Luther, Z. C. Holman and J. Huang, *Nat Photonics*, 2022, **16**, 588–594.

20 Q. Ma, W. Chu, S. Wu, Q. Wei, Z. Cheng, J. Wu, W. Liu, S. Ma, X. Ma, J. Chen and J. Dong, *Solar Energy*, 2022, **246**, 245–255.

21 T. Li, K. Mao, H. Meng, Z. Zhu, W. Peng, S. Yuan, J. Xu, X. Feng, Z. Xu and J. Xu, *Adv. Mater.*, 2023, **35**, 2211959.

22 J. Feng, X. Wang, J. Li, H. Liang, W. Wen, E. Alvianto, C. W. Qiu, R. Su and Y. Hou, *Nat. Commun.* , 2023, **14**, 1–8.

23 F. Wang, M. Li, Q. Tian, R. Sun, H. Ma, H. Wang, J. Chang, Z. Li, H. Chen, J. Cao, A. Wang, J. Dong, Y. Liu, J. Zhao, Y. Chu, S. Yan, Z. Wu, J. Liu, Y. Li, X. Chen, P. Gao, Y. Sun, T. Liu, W. Liu, R. Li, J. Wang, Y. bing Cheng, X. Liu, W. Huang and T. Qin, *Nat. Commun.* , 2023, **14**, 1–10.

24 L. Yan, H. Huang, P. Cui, S. Du, Z. Lan, Y. Yang, S. Qu, X. Wang, Q. Zhang, B. Liu, X. Yue, X. Zhao, Y. Li, H. Li, J. Ji and M. Li, *Nat. Energy* , 2023, **8**, 1158–1167.

25 J. Xu, H. Chen, L. Grater, C. Liu, Y. Yang, S. Teale, A. Maxwell, S. Mahesh, H. Wan, Y. Chang, B. Chen, B. Rehl, S. M. Park, M. G. Kanatzidis and E. H. Sargent, *Nat. Mater.*, 2023, **22**, 1507–1514.

26 Q. Jiang, J. Tong, Y. Xian, R. A. Kerner, S. P. Dunfield, C. Xiao, R. A. Scheidt, D. Kuciauskas, X. Wang, M. P. Hautzinger, R. Tirawat, M. C. Beard, D. P. Fenning, J. J. Berry, B. W. Larson, Y. Yan and K. Zhu, *Nature*, 2022, **611**, 278–283.

27 Q. Tan, Z. Li, G. Luo, X. Zhang, B. Che, G. Chen, H. Gao, D. He, G. Ma, J. Wang, J. Xiu, H. Yi, T. Chen and Z. He, *Nature*, 2023, **620**, 545–551.

28 S. Zhang, F. Ye, X. Wang, R. Chen, H. Zhang, L. Zhan, X. Jiang, Y. Li, X. Ji, S. Liu, M. Yu, F. Yu, Y. Zhang, R. Wu, Z. Liu, Z. Ning, D. Neher, L. Han, Y. Lin, H. Tian, W. Chen, M. Stolterfoht, L. Zhang, W.-H. Zhu and Y. Wu, *Science*, 2023, **380**, 404–409.

29 H. Chen, S. Teale, B. Chen, Y. Hou, L. Grater, T. Zhu, K. Bertens, S. M. Park, H. R. Atapattu, Y. Gao, M. Wei, A. K. Johnston, Q. Zhou, K. Xu, D. Yu, C. Han, T. Cui, E. H. Jung, C. Zhou, W. Zhou, A. H. Proppe, S. Hoogland, F. Laquai, T. Filleter, K. R. Graham, Z. Ning and E. H. Sargent, *Nat.Photon.*, 2022, **16**, 352–358.

30 Z. Li, B. Li, X. Wu, S. A. Sheppard, S. Zhang, D. Gao, N. J. Long and Z. Zhu, *Science*, 2022, **376**, 416–420.

31 S. M. Park, M. Wei, J. Xu, H. R. Atapattu, F. T. Eickemeyer, K. Darabi, L. Grater, Y. Yang, C. Liu, S. Teale, B. Chen, H. Chen, T. Wang, L. Zeng, A. Maxwell, Z. Wang, K. R. Rao, Z. Cai, S. M. Zakeeruddin, J. T. Pham, C. M. Risko, A. Amassian, M. G. Kanatzidis, K. R. Graham, M. Grätzel and E. H. Sargent, *Science*, 2023, **381**, 209–215.

32 G. Li, Z. Su, L. Canil, D. Hughes, M. H. Aldamasy, J. Dagar, S. Trofimov, L. Wang, W. Zuo, J. J. Jerónimo-Rendon, M. M. Byranvand, C. Wang, R. Zhu, Z. Zhang, F. Yang, G. Nasti, B. Naydenov, W. C. Tsoi, Z. Li, X. Gao, Z. Wang, Y. Jia, E. Unger, M. Saliba, M. Li and A. Abate, *Science*, 2023, **379**, 399–403.

33 W. Peng, K. Mao, F. Cai, H. Meng, Z. Zhu, T. Li, S. Yuan, Z. Xu, X. Feng, J. Xu, M. D. McGehee and J. Xu, *Science*, 2023, **379**, 683–690.

34 R. Azmi, E. Ugur, A. Seitkhan, F. Aljamaan, A. S. Subbiah, J. Liu, G. T. Harrison, M. I. Nugraha, M. K. Eswaran, M. Babics, Y. Chen, F. Xu, T. G. Allen,

A. ur Rehman, C. L. Wang, T. D. Anthopoulos, U. Schwingenschlögl, M. De Bastiani, E. Aydin and S. De Wolf, *Science*, 2022, **376**, 73–77.

35 C. Li, X. Wang, E. Bi, F. Jiang, S. M. Park, Y. Li, L. Chen, Z. Wang, L. Zeng, H. Chen, Y. Liu, C. R. Grice, A. Abudulimu, J. Chung, Y. Xian, T. Zhu, H. Lai, B. Chen, R. J. Ellingson, F. Fu, D. S. Ginger, Z. Song, E. H. Sargent and Y. Yan, *Science*, 2023, **379**, 690–694.

36 C. Fei, N. Li, M. Wang, X. Wang, H. Gu, B. Chen, Z. Zhang, Z. Ni, H. Jiao, W. Xu, Z. Shi, Y. Yan and J. Huang, *Science*, 2023, **380**, 823–829.

37 P. Shi, Y. Ding, B. Ding, Q. Xing, T. Kodalle, C. M. Sutter-Fella, I. Yavuz, C. Yao, W. Fan, J. Xu, Y. Tian, D. Gu, K. Zhao, S. Tan, X. Zhang, L. Yao, P. J. Dyson, J. L. Slack, D. Yang, J. Xue, M. K. Nazeeruddin, Y. Yang and R. Wang, *Nature*, 2023, **620**, 323–327.

38 Z. Liang, Y. Zhang, H. Xu, W. Chen, B. Liu, J. Zhang, H. Zhang, Z. Wang, D. H. Kang, J. Zeng, X. Gao, Q. Wang, H. Hu, H. Zhou, X. Cai, X. Tian, P. Reiss, B. Xu, T. Kirchartz, Z. Xiao, S. Dai, N. G. Park, J. Ye and X. Pan, *Nature*, 2023, **624**, 557–563.

39 R. Chen, J. Wang, Z. Liu, F. Ren, S. Liu, J. Zhou, H. Wang, X. Meng, Z. Zhang, X. Guan, W. Liang, P. A. Troshin, Y. Qi, L. Han and W. Chen, *Nat. Energy* , 2023, **8**, 839–849.

40 H. Li, C. Zhang, C. Gong, D. Zhang, H. Zhang, Q. Zhuang, X. Yu, S. Gong, X. Chen, J. Yang, X. Li, R. Li, J. Li, J. Zhou, H. Yang, Q. Lin, J. Chu, M. Grätzel, J. Chen and Z. Zang, *Nat. Energy*, 2023, **8**, 946–955.

41 C. Luo, G. Zheng, F. Gao, X. Wang, C. Zhan, X. Gao and Q. Zhao, *Nat. Photon.*, 2023, **17**, 856–864.

42 Z. Li, X. Sun, X. Zheng, B. Li, D. Gao, S. Zhang, X. Wu, S. Li, J. Gong, J. M. Luther, Z. Li and Z. Zhu, *Science*, 2023, **382**, 284–289.

43 Z. Huang, Y. Bai, X. Huang, J. Li, Y. Wu, Y. Chen, K. Li, X. Niu, N. Li, G. Liu, Y. Zhang, H. Zai, Q. Chen, T. Lei, L. Wang and H. Zhou, *Nature*, 2023, **623**, 531–537.